Analytical prediction of large radius bending by circular approximation

Authors: Vitalii Vorkov*, Richard Aerens, Dirk Vandepitte and Joost R. Duflou

* - corresponding author, e-mail: vitalii.vorkov@kuleuven.be

Address: KU Leuven, Department of Mechanical Engineering, Celestijnenlaan 300B, 3001, Leuven, Belgium

Keywords Bending, Sheet metal, Springback, Analytical model, High-strength steel

Abstract An accurate analytical method is normally the preferred choice in engineering practice since this approach usually does not require additional software and can be applied for different situations. A number of analytical methods have been proposed for the air bending process, however, none of them has the capacity to deal with large radius bending. Large radius bending is characterized by a high ratio of the punch radius to the die opening and it is often applied for high-strength steels because of their limited bendability. This bending mode is used to fulfill the imposed level of maximum strain during the forming process. This contribution develops an analytical solution based on the assumption that the bent plate profile can be represented by two straight lines and a circular segment. Three different hardening laws – linear, Swift, and Aerens - are used for the bending moment calculation. Unit moment measurements are used in order to avoid extrapolation of hardening curves obtained by tensile testing. The model is compared with a wide range of experiments using the coefficient of determination, relative and absolute average errors, in addition to the mean standard error. The analytical prediction based on the circular approximation is found to be an accurate and robust tool for the calculation of the major bending characteristics for large radius air bending of high-strength steels.

1 Introduction

Air bending is a well-known process in sheet metal forming. For common materials, air bending is mostly used with small radius punches. This process is called conventional or small radius bending. The increasing industrial utilization of high-strength steels is causing a shift to the use of large radius punches. Based on tooling dimensions, large radius bending is defined as the forming process where the ratio of a punch radius to a die opening is larger than 1/4 [1]. The high-strength steels have limited cold formability, and the use of large radius punches is inevitable to restrict the strain level during forming.

Despite the availability of different calculation solutions, such as numerical and regression models, engineers in practice prefer analytical solutions. Analytical methods calculate the required parameters without finite element commercial software for the case of numerical calculations, or without a prerequisite in the form of an extensive experimental database, which is necessary for regression models. In addition, analytical models usually provide a solution in a fraction of the time of expensive finite element solutions.

Several researchers have modeled the air bending process by means of analytical methods. The theory and practice of the bending process are covered in the classical textbooks by Marciniak [2] and Lange [3], or in a more recent textbook by Altan and Tekkaya [4]. Altan et al. developed a computer code which takes into account the evolution of material characteristics throughout the bending process [5-8]. Aerens and Masselis studied a wide range of problems in air bending and discussed the concept of the

circular approximation [9]. De Vin et al. developed a process model for air bending and introduced the importance of variation of material parameters in small batch manufacturing [10,11]. Elkins and Sturges [12] developed a control method for small radius bending based on an analytical bending model.

However, these research contributions do not take into account some of the peculiarities of large radius bending. In particular, the gradual change of the loading scheme due to the multi-breakage effect is not properly addressed. The authors already investigated the problem of large radius bending by means of experimental [1,13,14], numerical [15-17], and regression approaches [18,19].

This contribution aims to develop a simple analytical method that predicts the bending characteristics in a fast and reliable way. The following structure is used in order to achieve this aim. Section 2 describes major characteristics of large radius bending. The next section presents the analytical formulas based on the circular approximation with particular attention to contact points position in Section 3.1, bending moment in Section 3.2, bending force in Section 3.3, springback in Section 3.4, and bend allowance in Section 3.5. Section 4 briefly introduces an experimental procedure used for the data acquisition. Comparison of calculated values for all considered bending characteristics with experimental results and discussion of the prediction accuracy are presented in Section 5. The last section provides the final remarks and conclusions.

2 Bending characteristics

The focus of this work is on the analytical determination of the most important bending characteristics, namely: bending force, springback, and bend allowance. During the bending process with large radius punches the loading scheme changes gradually due to the multi-breakage effect [20], this effect is important and must be taken into account in the prediction model because it drastically affects the bending moment and consequently the bending force and springback. This effect is described by the distance l_c between the contact points (Figure 1a) and by the distribution of the bending moment, as represented in Figure 2. The bending force is an important indicator for the user. It characterizes the required capacity of the press brake and it warns the user in case of tooling damage.

Springback $\Delta\beta$ (Figure 1b) is considered as the most important bending characteristic as it characterizes the final shape of the bent plate. Springback is the change of angle due to the release of the elastic deformation after the forming process, it is defined as the difference between the final product angle β' and the imposed bending angle β. Finally, the bend allowance *BA* allows to determine the initial dimensions of the flat pattern before forming. This bending characteristic is calculated as the difference between the initial length of the blank l_0 and the sum of the bent flanges l_1 and l_2 (Figure 1c).

3 Circular approximation model

For conventional bending, i.e. with a small punch radius, the punch is in contact with the plate in a narrow area and the neutral line of the plate follows a specific curve, which can be approximated by a spline or by a piecewise function. However, for large radius bending, the punch is in contact with the plate over a relatively wide arc and next to this curved segment, the plate maintains a much flatter shape. This observation seems to justify a circular approximation of the large radius bending, an assumption that will be investigated in this contribution.

The circular model approximates the bent shape as the union of two straight lines with a circular segment in between. The projections of the contact points on the neutral line are the points that split the bent plate into these two distinct regions. Examples of bent samples are shown in Figure 3. The circular approximation does not provide a perfect fit, but for the construction steel St-37 (Figure 3a) and for the high-strength steel Strenx 1300 (Figure 3b), this approximation closely resembles the real bent shape. Other materials used in this work revealed the similar observations. Therefore, this shape is used in the analytical model.

The profile description of the circular approximation model is shown in Figure 4a. The reaction forces and their levers are given in Figure 4b. This paper further refers to the angles θ and θ' as half of the complement to the bending angle β and the product angle β' respectively. For the calculation of the bending characteristics, the neutral fiber is assumed to lie in the middle of the plate [4] throughout the forming process.

The curved part of the plate is modeled as a circle segment, therefore the radius of curvature of the neutral line R_A is equal to the punch radius R_p plus half the thickness of the plate. Figure 4a shows that the circular l_a and straight l_d segments can be calculated as:

$$l_a = \theta \cdot R_A \qquad (1)$$

$$l_d = \frac{w}{2\,cos\theta} - (R_d + t/2 + R_A) \cdot tan\theta \qquad (2)$$

where w is the distance between the centers of the die shoulders, which (see Figure 4c) can be evaluated as a function of the commercial definition of the die opening w_0:

$$w = w_0 + 2R_d\,tan(45 - \frac{\alpha_d}{4}) \qquad (3)$$

where R_d is the die radius and α_d the die angle in degrees.

3.1 Contact points position

In the assumption that the plate is wrapped around the punch, the position of the contact points (Figure 1a) for the circular approximation is found by the simple equation:

$$l_c = \theta \cdot R_p \qquad (4)$$

In addition to the loading scheme, the value of the measured contact length is important for the validation of the circular approximation model.

3.2 Determination of the bending moment

The value of the bending moment is the key parameter for the validity of the prediction of the bending characteristics. Assuming that the neutral fiber lies in the middle of the plate, the bending moment per unit width M'_b along the cross-section can be obtained as:

$$M'_b = 2\int_0^{t/2} \sigma_x(y) \cdot y \cdot dy \qquad (5)$$

where t is the plate thickness, y the coordinate through the plate thickness (having as origin the middle of the plate) and $\sigma_x(y)$ the stress normal to the section.

Since the stress is expressed as a function of the strain, it is convenient to switch from variable y to variable strain ε_x. As $y = \varepsilon_x \cdot R_A$, the bending moment per unit width in point A can be written as:

$$M'_A = \frac{t^2}{2\varepsilon_b^2}\int_0^{\varepsilon_b} \sigma_x(\varepsilon_x)\,\varepsilon_x\,d\varepsilon_x \qquad (6)$$

where $\varepsilon_b = t/(2R_A)$ is the bending strain.

The unit moment σ_A^* (Equation 7) can be obtained by dividing Equation 6 by t^2. In this case on the left side of Equation 7, besides the bending moment, we obtain only plate dimensions (width and thickness) and on the right side, there are only material parameters. The unit moment can be measured directly.

$$\sigma_A^* = \frac{M'_A}{t^2} = \frac{M_A}{b\,t^2} = \frac{1}{2\varepsilon_b^2}\int_0^{\varepsilon_b} \sigma_x(\varepsilon_x)\,\varepsilon_x\,d\varepsilon_x \qquad (7)$$

Since bending occurs in a plane strain configuration, assuming a Von Mises criterion and neglecting the radial stress σ_y [2], we have:

$$\sigma_x = \frac{2}{\sqrt{3}}\sigma_f \qquad (8)$$

$$\varepsilon_x = \frac{\sqrt{3}}{2}\varepsilon_f \qquad (9)$$

where σ_f and ε_f are the flow stress and the representative plastic strain respectively, which are identical to the stress σ and strain ε measured during tensile testing i.e. the hardening law $\sigma(\varepsilon)$.

One of the simplest representations of the hardening behavior is the linear law (Equation 10 and Figure 5a). Despite its simplicity, it allows describing the hardening behavior of some materials like AISI 304 and Strenx 700 MC, as can be seen in Figure 7 and Figure 8. The Swift model (Equation 11 and Figure 5b) allows describing the hardening behavior of the construction and stainless steels accurately, as illustrated in Figure 6 and Figure 7.

Figure 9 shows that the Swift model does not allow to provide an accurate approximation for Strenx 1300 and thus another model should be applied. We propose to use the Aerens model, which is a modified Swift model: it allows to describe the hardening curve taking into account the smooth transition between the elastic and plastic zones; it has the form of Equation 12. Figure 8 and Figure 9 show the possible fit of the tensile data with the three above-mentioned hardening laws. The Aerens model shows clear superiority for the fitting of the hardening behavior of Strenx 1300 in comparison with the Swift model. This model should not be applied to the construction steel St-37 and the stainless steels AISI 304 and AISI 316L because these materials show no or only a negligible transition zone. Using this law for these materials brings about an unnecessary complexity (in this case, $k = \infty$ which reduces Equation 12 to the Swift model), and thus its usage is inappropriate.

Further, the Swift and linear models are applied to all materials, and the Aerens model is used only for the high-strength steels Strenx 700 MC and Strenx 1300. Table 1 and

Table 2 present the material parameters for the above-mentioned hardening models, and the stabilized value of the secant elasticity modulus E_{sec}. The linear model reads

$$\sigma = A + B \cdot \varepsilon \qquad (10)$$

where A and B are the material parameters for the linear law.

The Swift model reads

$$\sigma = K_S \cdot (\varepsilon + \varepsilon_{0S})^{n_S} \qquad (11)$$

where K_S is the strength coefficient, n_S the hardening exponent, ε_{0S} the initial strain.

The Aerens model reads

$$\sigma = \left[1 - e^{-k\cdot(\varepsilon-\varepsilon_{el})}\right][K_A \cdot (\varepsilon + \varepsilon_{0A})^{n_A} - \sigma_{el}] + \sigma_{el} \quad (12)$$

where K_A is the strength coefficient, n_A the hardening exponent, ε_{0A} the initial strain, ε_{el} the elastic strain limit, σ_{el} the elastic stress limit, and k is defined as:

$$k = \frac{E}{K_A\cdot(\varepsilon_{el}+\varepsilon_{0A})^{n_A}-\sigma_{el}} \quad (13)$$

After the integration of Equation 7 with the linear hardening law (Equation 10) and the Swift law (Equation 11), and taking into account the plane strain state (Equation 8 and Equation 9), the resulting equations for the unit moment at point A (Figure 4a) can be found as:

$$\sigma_A^* = \frac{A}{2\sqrt{3}} + \frac{2}{9}B\varepsilon_b \quad (14)$$

$$\sigma_A^* = \left(\frac{2}{\sqrt{3}}\right)^{n_S+1} \frac{K_S}{2\cdot\varepsilon_b^2} \cdot \left(\frac{(\varepsilon_b+\varepsilon_{0S})^{n_S+2}-\varepsilon_{0S}^{n_S+2}}{n_S+2} - \frac{\varepsilon_{0S}\cdot((\varepsilon_b+\varepsilon_{0S})^{n_S+1}-\varepsilon_{0S}^{n_S+1})}{n_S+1}\right) \quad (15)$$

According to [9], Equation 15 can be simplified:

$$\sigma_A^* = \left(\frac{2}{\sqrt{3}}\right)^{n_S+1} \frac{K_S}{2(n_S+2)} \cdot (\varepsilon_b + \varepsilon_d)^{n_S} \quad (16)$$

$$\varepsilon_d = \varepsilon_{0S} \cdot (1 + n_S/2)^{1/n_S} \quad (17)$$

With the Aerens model (Equation 12), Equation 7 cannot be integrated analytically; therefore, its integration has to be performed numerically in order to obtain the value of the unit moment.

As it can be seen from Figure 8 and Figure 9, the hardening curves for Strenx 700 MC and Strenx 1300 stop at strains of about 4%, as this is the limit of the achieved plastic strain by means of tensile testing. However, for the bending tests conducted in this work, strains up to 28% could be achieved, thus it was necessary to directly measure the unit moment in order to have reliable data for the high-strength materials. As practice shows, the level of the strain in the unit moment measurement is a lot higher than for the tensile testing. The usage of the unit moment allows avoiding undesirable issue of extrapolation.

For the measurement of the unit moment specific equipment is required [22-24]. The unit measurement device has been developed by R. Aerens [9,22] and has been used to perform measurements for Strenx 700 MC (Figure 10) and Strenx 1300 (Figure 11). The measured unit moment curves have the same appearance as the tensile curves. Therefore, the unit moment curves have been fitted according to Swift-like and Aerens-like hardening laws. The Swift-like equation is Equation 16 and the Aerens-like equation is Equation 18.

$$\sigma_A^* = \left[1 - e^{-k_b\,(\varepsilon_b-\varepsilon_{b\,el})}\right][C''\,(\varepsilon_b + \varepsilon_d)^n - \sigma_{el}^*] + \sigma_{el}^* \quad (18)$$

where k_b is defined as:

$$k_b = \frac{E_b}{C''(\varepsilon_{b\,el}+\varepsilon_d)^n-\sigma_{el}^*} \quad (19)$$

where $\varepsilon_{b\,el}$ is the limit of elastic bending strain, σ^*_{el} is the limit of elastic unit moment, E_b is the slope of the elastic unit moment.

The corresponding material characteristics are reported in

Table 3 and

Table 4 with the corresponding curves are depicted in Figure 10 and Figure 11.

3.3 Bending force

The normal and tangential forces and their levers from point C are shown in Figure 4b. In the assumption that the plate is wrapped around the punch, the curvature of the plate is constant between points A and C, and thus the levers can be found as:

$$b_{lev} \equiv l_d \quad (20)$$

$$b_{lev2} \equiv t/2 \quad (21)$$

The bending moment that is required for this magnitude of deformation is constant in the plate segment between points A and C:

$$M_A = F_n b_{lev} + F_t b_{lev2} \quad (22)$$

Considering the Coulomb friction model with a friction coefficient μ, the relation between F_t and F_n is specified as:

$$F_t = \mu F_n \quad (23)$$

The value of the normal force can be found by inserting Equation 23 into Equation 22:

$$F_n = \frac{M_A}{b_{lev} + \mu\, b_{lev2}} \quad (24)$$

Finally, the sum of projections of the friction (Equation 23) and normal (Equation 24) forces on the vertical axis defines the bending force in the form of:

$$F_b = 2F_n \cos\theta \cdot (1 + \mu \tan\theta) \quad (25)$$

3.4 Springback

The springback angle is calculated with the elastic formula:

$$\Delta\beta = \frac{1}{E'I} \int_0^{l_{tot}} M\, dl \quad (26)$$

where l is a curvilinear axis formed by the neutral line, $I=bt^3/12$ the second moment of area about the middle axis and $E'=E/(1-\nu^2)$ the elasticity modulus in the plane strain mode where v is the Poisson ratio.

The circular approximation assumes that the elastic deformations are zero on a circular segment and that only elastic strains are present in both straight segments. Taking into account these assumptions, plastic strains in straight segments are zero, whereas plastic deformations are constant along the circular segment. Given this difference in the plastic strain level, it is reasonable to assume that these regions should have been assigned different values of the elasticity modulus based on the plastic pre-strain. The change of the elasticity modulus due to pre-strain showed a significant influence on the accuracy of the springback prediction [25,26]. Figure 12 shows the deformation scheme and bending moment diagram, which are used for the springback prediction.

The drop of elasticity modulus due to previously applied deformation or pre-strain is approximated using the so-called secant elasticity modulus, as defined in Figure 13. The evolution of the secant elasticity modulus versus the pre-strain in the case of Strenx 700 MC, as example, is given in Figure 14 [17].

Finally, the springback according to the circular approximation can be calculated by integration of Equation 26 and using the elasticity modulus corresponding to the predefined regions (Figure 12b) and using the bending moment per unit width or the unit moment:

$$\Delta\beta = \frac{12 \cdot M'_A}{t^3}\left(\frac{2 \cdot l_a}{E'_{sec}} + \frac{l_d}{E'}\right) \quad (27)$$

where M'_A is the bending moment per unit width in A.

$$\Delta\beta = \frac{12 \cdot \sigma^*_A}{t}\left(\frac{2 \cdot l_a}{E'_{sec}} + \frac{l_d}{E'}\right) \quad (28)$$

where σ^*_A is the unit moment in A.

3.5 Bend allowance

The bend allowance is the difference between the original length and the sum of the lengths of the bent flanges. However, according to the circular approximation, the plate outside the contact points is straight, and thus for the bend allowance calculation, we can consider only the region between the two contact points (Figure 15).

The inner radius of the bent plate before the springback is known and equal to the punch radius; however, the inner radius after springback is unknown. Assuming that the same region remains deformed after springback, we can calculate the final plate radius by equating the arc length of the bent plate l_a before (Figure 15a) and after (Figure 15b) springback. As the result, the radius after the springback is equal to:

$$R_{BA} = R_A \frac{\theta}{\theta'} \quad (29)$$

The difference between the middle line of the circular segment l_a and the line l_{BA} provides the value of the bend allowance (Figure 15b). This value is calculated as follows:

$$BA = 2\theta' R_{BA} - 2(R_{BA} + t/2) \cdot tan\,\theta' \quad (30)$$

This is the well-known formula from DIN 6935 in the case of the neutral fiber lying in the middle of the plate.

4 Experimental investigation

This section provides a brief description of used plates, materials and tooling. The complete description is available in [1] where experimental procedure, measurement methods, variability and reproducibility of the large radius bending is discussed in detail. A full factorial test plan with one repetition per test case has been implemented. For some test cases several repetitions have been executed in order to study process variability. In case of several repetitions, the average values have been used as the resulting values.

Large radius bending is most often applied to high-strength steels with limited cold formability. Two materials of this type are selected for validation purposes: Strenx 700 MC and Strenx 1300. In addition to high-strength steels, the standard construction steel St-37 (or S235JR), and the stainless steels AISI 304 and AISI 316L have been used in this study to verify the applicability of the analytical model for common sheet metal steels. This selection of materials allows for the evaluation of the quality of the analytical prediction based on the circular approximation model. The Coulomb friction coefficient (Equation 25) of 0.2 has been selected for all materials except Strenx 1300 for which the value of 0.3 has been chosen. This choice is based on the previous calculations [1] and measurements performed on coarse and smooth materials [9].

In addition to the different materials, punches with different radii, dies with different openings, and plates with different thicknesses have been selected for verification purposes. Figure 16 presents an overview of the tooling and plates. Experiments are restricted to configurations that are physically possible (e.g. a die opening should be bigger than a punch diameter). In most combinations, four bending angles β (Figure 1a) have been executed: 90°, 110°, 130°, and 150°.

Table 5 presents an experimental plan that results in 515 bending tests. For some cases, repetitions are included to be able to assess the reproducibility of the experiments. The complete description of the experimental procedure can be found in [1], and the complete experimental data are available via the Dataverse scientific data repository in [27].

It should be mentioned that air bending, in general, has a rather large variation of the resulting bending characteristics. This variation is usually caused by an imperfect measuring procedure [1,28] and by the natural scatter of the material properties [10,29]. For instance, a variation of 1° for the bending angles is quite common for high-strength steels. This aspect should also be taken into account when assessing the prediction quality of the developed model. More detailed information about variability and reproducibility the reader can find in [1,28] and maximal standard errors for each bending characteristic is listed in

Table 7.

5 Results and discussion

In order to estimate the accuracy of the circular approximation model used for the prediction of large radius bending, the calculated results were compared to 515 experimental points (

Table 5) [1,27]. The accuracy of the proposed approach has been measured with three indicators: the coefficient of determination R^2, the average absolute error ε_{av} (Equation 31), and the relative error ε_{rel} (Equation 32). Additionally, in order to estimate the bias of the prediction model, the average error $\bar{\varepsilon}_{av}$ (Equation 33) and the standard error of the mean $\sigma_{\bar{\varepsilon}_{av}}$ (Equation 34) have been calculated.

$$\varepsilon_{av} = \left(\sum_{i=1}^{n} \left| v_i^{Exp} - v_i^{A} \right| \right)/n \qquad (31)$$

where v_i^{Exp} and v_i^{A} are experimental and analytical data respectively, n the number of comparisons.

$$\varepsilon_{rel} = \sum_{i=1}^{n} \left| v_i^{Exp} - v_i^A \right| / \sum_{i=1}^{n} v_i^{Exp} \quad (32)$$

$$\bar{\varepsilon}_{av} = \left(\sum_{i=1}^{n} v_i^{Exp} - v_i^A \right) / n \quad (33)$$

$$\sigma_{\bar{\varepsilon}_{av}} = s/n \quad (34)$$

where *s* is the sample standard deviation.

The verification procedure includes four different attributes of the bending process, namely the position of the contact points, the magnitude of bending force, the magnitude of springback and the bend allowance. The final correlation criterion is the bias of the prediction model. Prediction models based on the unit moment measurement are used with "UM" label further in the text.

5.1 Contact points position

Equation 4 provides a prediction of the contact points position. The comparison parameters show that the assumption of the circular approximation is valid for the determination of the loading scheme in large radius air bending. Figure 17 and Figure 18 show examples of the comparison between experimental data and prediction according to Equation 4.

Table 7 provides an overview of the comparison parameters.

5.2 Bending force

Equation 25 provides a prediction of the bending force. It almost always gives slightly overestimated values and this overestimation allows for a conservative and safe prediction.

For construction and stainless steels, the Swift and linear models give a comparable prediction. This is explained by very similar approximations of the hardening behavior (Figure 6 and Figure 7). For high-strength steels, the Aerens and Swift models based on tensile tests and unit moment tests give a better prediction compared to the linear model. This is confirmed by the larger value of R^2 and smaller values of the average absolute error ε_{av} and relative error ε_{rel}.

The results for unit moment models are a lot better for Swift UM model than the results for Swift based on tensile tests: 9.9% of ε_{rel} instead of 18.4% for Strenx 700 MC. Also, the Aerens model with unit moment curve is also performed better than the extrapolated Aerens model: 16.6% of ε_{rel} instead of 19.6%. R^2 in this case can be misleading, since its value almost equal and very high for all cases. And as was state before, all methods show the significant overestimation bias.

The summary of the prediction quality parameters for the bending force is presented in

Table 8 and examples of comparison between experiments and calculated values are shown in Figure 19 and Figure 20.

5.3 Springback

Figure 21 and Figure 22 present examples of the comparison between calculated and measured values for the springback. Equation 27 assumes the moment distribution depicted in Figure 12b, which is only a hypothesis. Still, for the high-strength steels, the model with this kind of the moment distribution delivers results with high values of coefficient of determination R^2: Strenx 700 MC – 0.93, Strenx 1300 – 0.98, with the average error ε_{av} below 0.6°. The Swift model based on the tensile curves again outperformed by the Swift UM model: ε_{rel} 15.8% and 4.01% correspondingly for Strenx 1300. Both

Aerens models deliver similar prediction values for springback angle and additionally show virtually no bias of the prediction error.

For the conventional steels, the values of R^2 are lower (St-37 – 0.82, stainless – 0.90), but the average absolute errors are less or slightly more than 1° and taking into account the variability and reproducibility [1,28] of air bending, these values can be accepted. These errors can be caused, for instance, by the difference in material properties of the bending samples.

Prediction of the springback is a notoriously intricate task, and it is usually assumed that for a correct prediction, an elaborate material characterization is required. However, the developed model provides an accurate prediction based only on a limited number of materials parameters obtained from standard tensile testing. Equation 27 offers a prediction of the springback and Table 9 provides an overview of the comparison parameters for different materials.

5.4 Bend allowance

Table 10 presents an overview of the comparison between experimental results and predicted values according to Equation 30. The bend allowance is highly affected by the springback (Equation 29) since the determination of the resulting bending radius requires the knowledge of the final angle. Therefore, inaccurate values of the springback increase the error in the bend allowance prediction. Figure 24 and Figure 25 show examples of the comparison for St-37 and Strenx 1300 respectively.

The strength (e.g. yield strength) and the hardening exponent of the considered material also play important roles in the bend allowance calculation. Figure 23 shows clear tendencies for these two parameters: lower hardening exponent and higher yield strength result in lower relative errors. These trends are indicated by the dashed lines in Figure 23.

Table 10 shows that the values of the average absolute errors are smaller for the high-strength steels with high values of yield stresses and lower values of hardening exponents. It seems that the assumption of straight lines outside of the deformation zone has a better correspondence to reality for these steels. The added error for the conventional steels is brought about by the additional deformation of the segments outside of the contact zone. Therefore, the prediction for St-37 and AISI 304/AISI 316 steel is rather inaccurate, since the error is less than 1.3 mm for these steels and may not be suitable for process planning or CAM purposes.

For the high-strength steels, the analytical formula provides more accurate values for the bend allowance: for Strenx 700 MC, an average error less than 0.9 mm, and for Strenx 1300, an average error less than 0.4 mm. Again, the superior prediction quality for Strenx 1300 seems to be due to the lower deformation of the straight segments. Additionally, high-strength steels show limited overestimation bias below 0.5 mm.

6 Conclusions

This contribution describes an analytical prediction model for large radius bending with a circular approximation. This analytical model delivers a robust and accurate prediction tool for large radius bending of high-strength steels for all major bending characteristics: bending force, springback, and bend allowance. This is confirmed by comparing the developed model with a wide range of experimental results. The model accuracy also justifies a circular approximation as a valid assumption

for the prediction of the large radius bending for high-strength steels. It should be mentioned that for conventional materials, the prediction is not always satisfactory, thus the developed model is advisable to apply for high-strength steels.

The model validation is based on the R^2 statistics and on the average absolute and relative errors. Moreover, the bias of the prediction model has been analyzed for all bending characteristics. Based on the circular approximation assumption, the values of the contact points position is mostly always overestimated. This overestimation consequently leads to enlarged bending moment. The prediction of the bending force is also overestimated, as confirmed by the negative values of the average error parameter. However, springback and bend allowance of high-strength steels show very little bias given the correct estimation of the bending moment by Aerens law.

Estimation of the bending moment is a crucial parameter for the prediction of the bending characteristics. For the correct calculation of the bending moment, an appropriate hardening model and valid hardening curves are required. Aerens law allows to fit the hardening behavior of high-strength steels accurately including the transition zone between elastic and plastic regions. Additionally, the bending moment based on unit moment measurements allows to avoid extrapolation of hardening curves and deliver more accurate and reliable results when compare to bending moment calculated from extrapolated values.

The proposed model delivers an analytical solution, which requires only limited information about the material, which is contained in the stress-strain response from the common tensile testing procedure. These data can be requested from the material supplier or they can routinely be obtained in almost any material testing laboratory.

References

1. Vorkov V, Aerens R, Vandepitte D, Duflou JR (2017) Experimental investigation of large radius air bending. Int J Adv Manuf Technol 92 (9):3553-3569
2. Marciniak Z, Duncan JL (1992) Mechanics of sheet metal forming. Edward Arnold, Great Britain
3. Lange K (1985) Handbook of metal forming. McGraw-Hill Book Company, New York
4. Altan T, Tekkaya AE (2012) Sheet metal forming: processes and applications. Asm International, USA
5. Kim H, Nargundkar N, Altan T (2007) Prediction of bend allowance and springback in air bending. J Manuf Sci E-T ASME 129 (2):342-351
6. Wang C, Kinzel G, Altan T (1993) Mathematical modeling of plane-strain bending of sheet and plate. J Mater Process Technol 39 (3):279-304
7. Yang X, Choi C, Sever NK, Altan T (2016) Prediction of springback in air-bending of advanced high strength steel (DP780) considering Young's modulus variation and with a piecewise hardening function. Int J Mech Sci 105:266-272
8. Yang X, Kardes N, Choi C, Taylan A (2011) Investigating springback in bending of advanced high-strength steel, Part II Springback prediction. STAMPING Journal January/February:8-9
9. Aerens R, Masselis S (2000) Air bending. Scientific and Technical Research Center of the Metal Fabrication Industry (CRIF/WTCM/SIRRIS) MC 110, Leuven, Belgium
10. De Vin LJ, Streppel AH, Kals HJJ (1994) Tolerancing and sheet bending in small batch part manufacturing. CIRP Ann - Manuf Technol 43 (1):421-424
11. De Vin LJ, Streppel AH, Singh UP, Kals HJJ (1996) A process model for air bending. J Mater Process Technol 57 (1-2):48-54

12. Elkins KL, Sturges RH (1999) Springback Analysis and Control in Small Radius Air Bending. J Manuf Sci E-T ASME 121 (4):679-688. doi:10.1115/1.2833103
13. Vorkov V, Aerens R, Vandepitte D, Duflou JR (2015) Influence of a single bend in the bumping process of large radius air bending. Key Eng Mater 651:1090-1095
14. Vorkov V, Aerens R, Vandepitte D, Duflou JR (2015) On the identification of a loading scheme in large radius air bending. Key Eng Mater 639:155-162
15. Vorkov V, Aerens R, Vandepitte D, Duflou JR (2014) Springback prediction of high-strength steels in large radius air bending using finite element modeling approach. Procedia Eng 81:1005-1010
16. Vorkov V, Konyukhov A, Vandepitte D, Duflou JR (2016) Contact modeling of large radius air bending with geometrically exact contact algorithm. Journal of Physics: Conference Series 734
17. Vorkov V, Vandepitte D, Duflou JR Finite element modeling of large radius bending operation (submitted). Int J Manufacturing Research
18. Vorkov V, Aerens R, Vandepitte D, Duflou JR (2017) Accurate prediction of large radius air bending using regression. Procedia Eng 207:1623-1628
19. Vorkov V, Aerens R, Vandepitte D, Duflou JR (2018) Two regression approaches for prediction of large radius air bending. Int J Mater Form. doi:10.1007/s12289-018-1422-7
20. Vorkov V, Aerens R, Vandepitte D, Duflou JR (2014) The multi-breakage phenomenon in air bending process. Key Eng Mater 611:1047-1053
21. Samuel KG, Rodriguez P (2005) On power-law type relationships and the Ludwigson explanation for the stress-strain behaviour of AISI 316 stainless steel. J Mater Sci 40 (21):5727-5731
22. Aerens R (1997) Characterisation of material by bending. Proceedings of the fifth International Conference on Sheet Metal: SheMet'97:251-262
23. Perduijn AB, Hoogenboom SM (1995) The pure bending of sheet. J Mater Process Technol 51 (1):274 - 295
24. Hoefnagels JPM, Ruybalid AP, Buizer CA (2015) A Small-Scale, Contactless, Pure Bending Device for In-situ Testing. Exp Mech 55 (8):1511-1524
25. Chatti S, Fathallah R (2012) A study of the variations in elastic modulus and its effect on springback prediction. Int J Mater Form:1-11
26. Wagoner RH, Lim H, Lee M-G (2013) Advanced issues in springback. Int J Plast 45:3-20
27. Vorkov V (2017) Complete experimental data for large radius bending. doi:10.7910/DVN/P7XKVV, The Dataverse project
28. Vorkov V (2017) Variability data for large radius bending. doi:10.7910/DVN/WJGDUR, The Dataverse project
29. Streppel AH, De Vin LJ, Brinkman J, Kals HJJ (1993) Suitability of sheet bending modelling techniques in CAPP applications. J Mater Process Technol 36 (3):339-356

Figure list

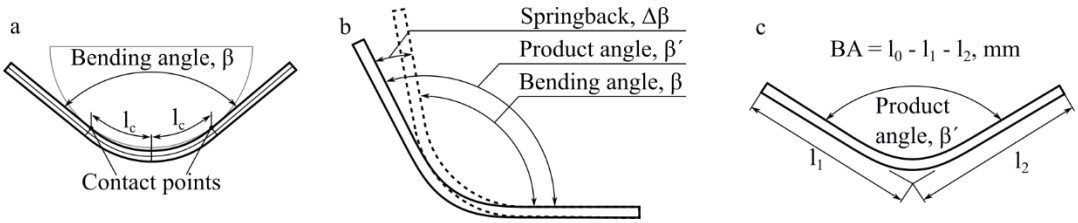

*Figure 1 – Bending characteristics: **a**) contact point positions; **b**) forming angles and springback; **c**) bend allowance, where l_0 is the initial plate length.*

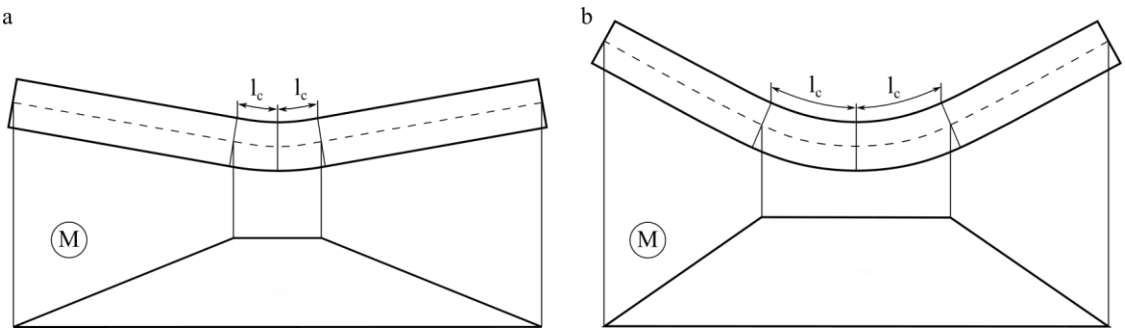

Figure 2 – Contact point positions and their influence on the bending moment.

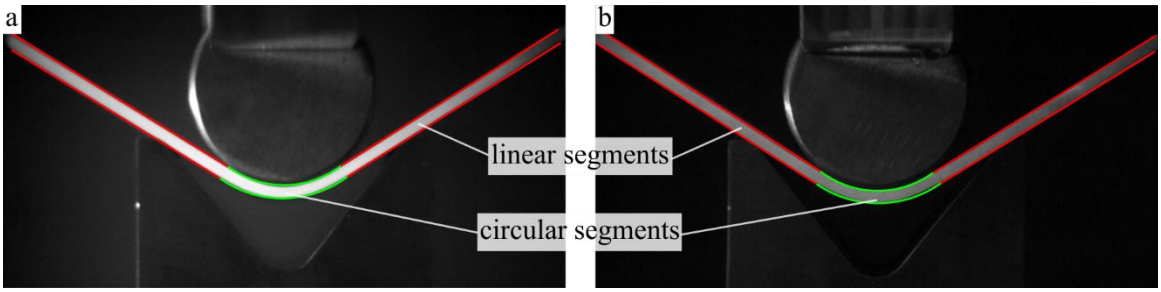

*Figure 3 – The circular model closely resembles the bent profile for the construction steel St-37 (**a**) and for the high-strength steel Strenx 1300 (**b**).*

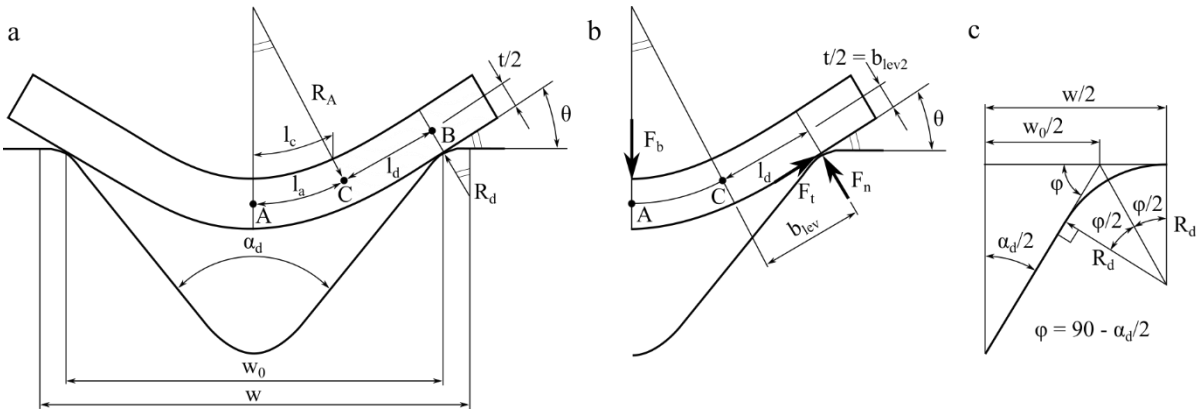

*Figure 4 - Circular approximation model for large radius bending: **a**) geometrical scheme; **b**) forces and their levers; **c**) die opening calculation.*

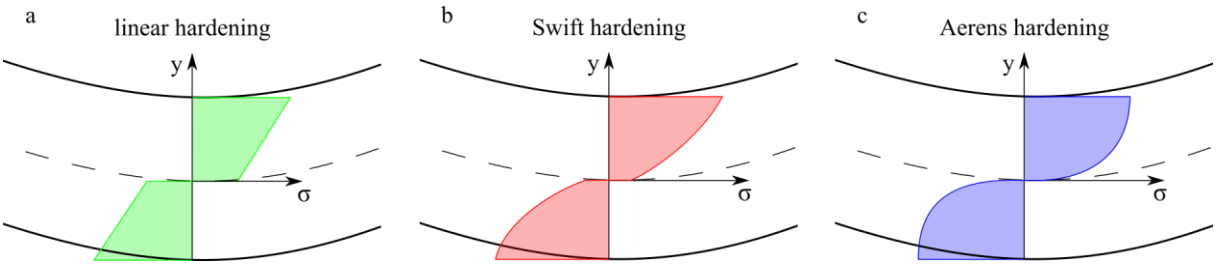

Figure 5 – Representation of the stress distribution through the thickness for different models of work hardening.

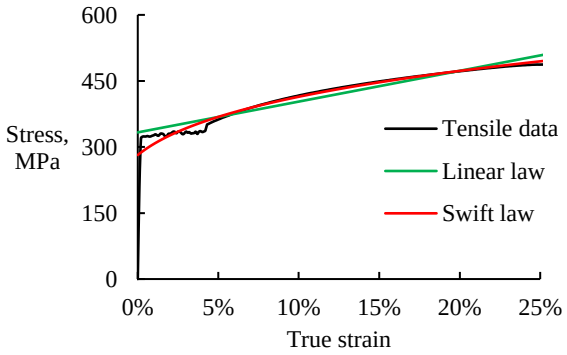

Figure 6 – Stress-strain curves for St-37.

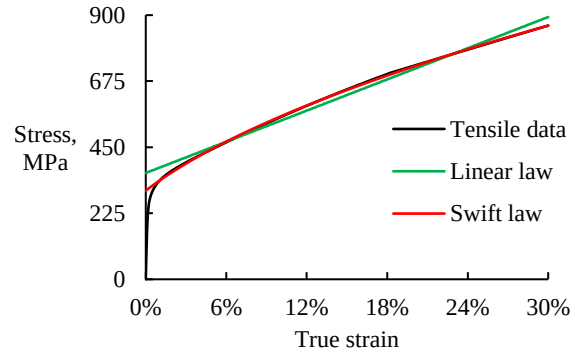

Figure 7 – Stress-strain curves for AISI 304.

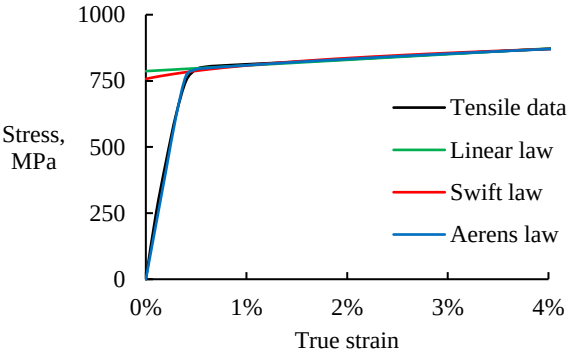

Figure 8 – Stress-strain curves for Strenx 700 MC.

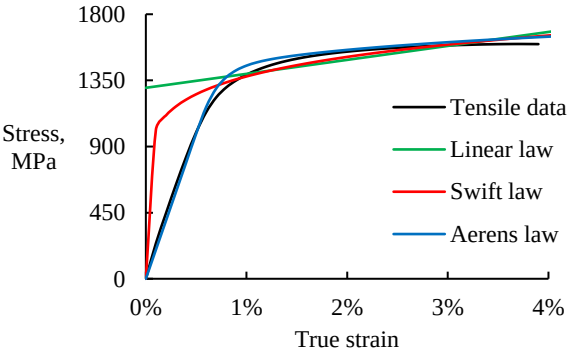

Figure 9 – Stress-strain curves for Strenx 1300.

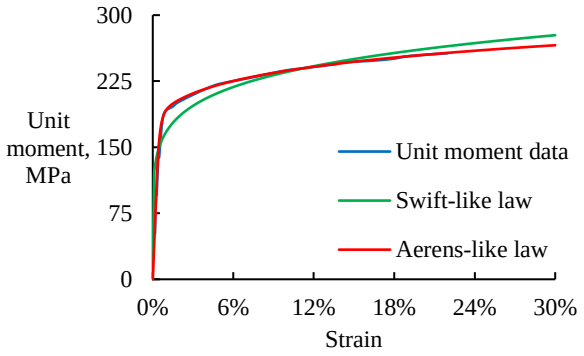

Figure 10 – Unit moment for Strenx 700 MC.

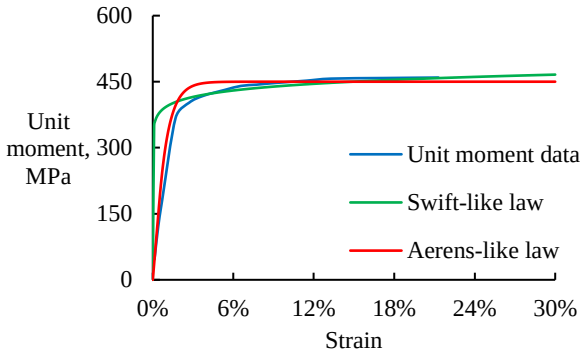

Figure 11 – Unit moment for Strenx 1300.

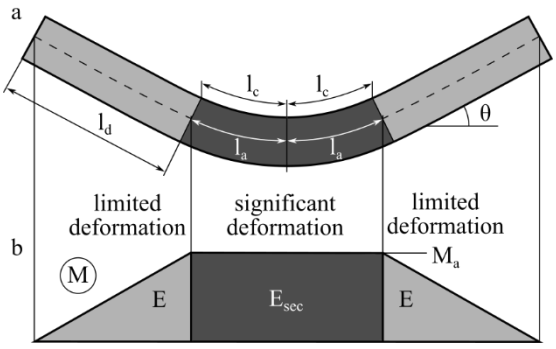

*Figure 12 – **a**) Division of the bent plate according to the strain levels; **b**) approximation of the bending moment for the large radius air bending, with the depiction of the assigned values of the elasticity modulus.*

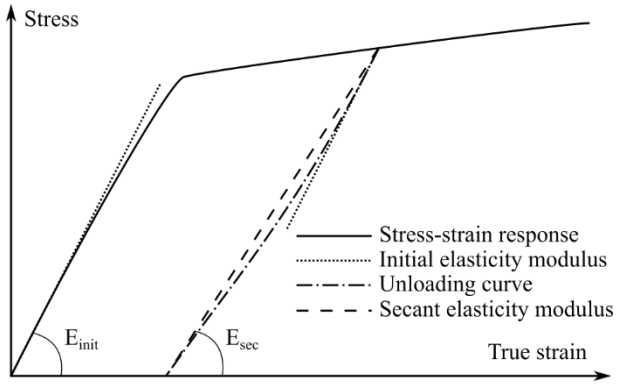

Figure 13 – Definition of secant elasticity modulus E_{sec} and initial elasticity modulus E_{init}.

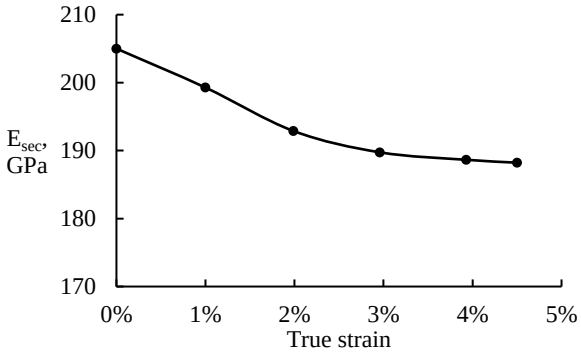

Figure 14 – Evolution of E_{sec} versus the pre-strain.

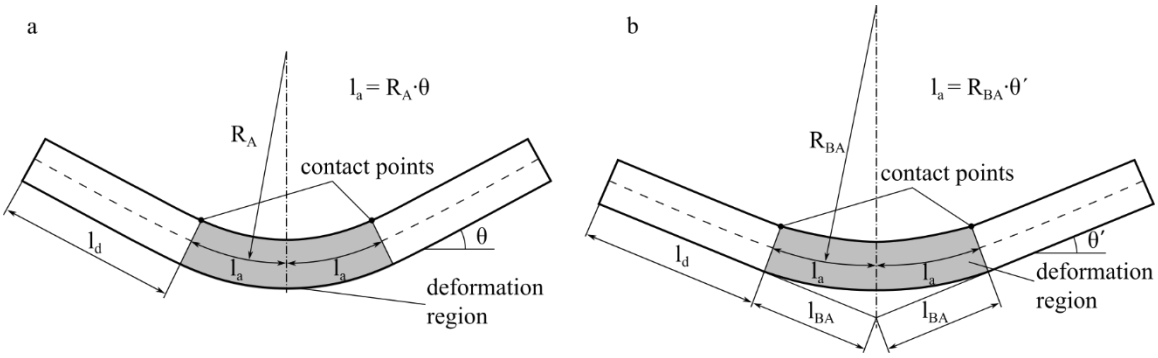

*Figure 15 – Scheme for the determination of the bend allowance. The plate shape (**a**) before and (**b**) after springback.*

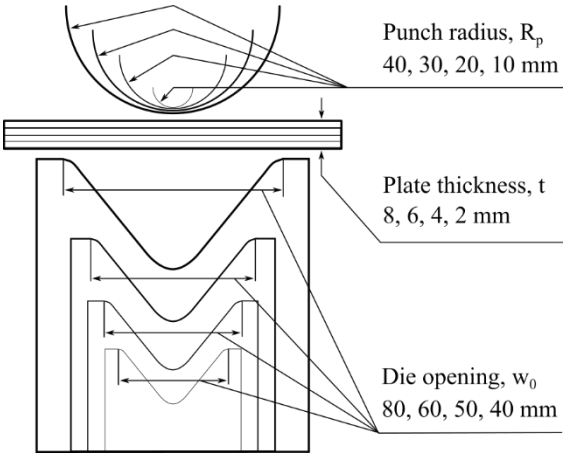

Figure 16 – Overview of used plates and tooling.

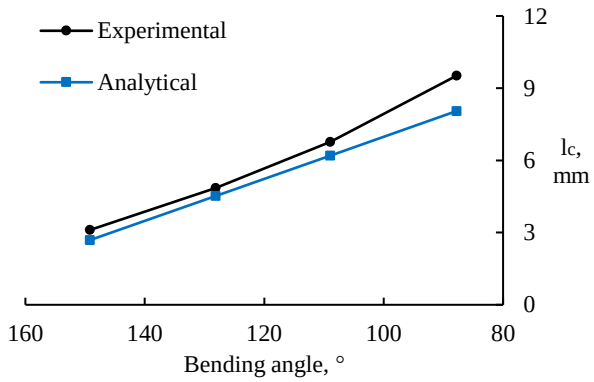

Figure 17 – Comparison of results for contact points position between analytical model and experimental data. Plate: AISI 316L; thickness: 8 mm; die opening: 50 mm; punch radius: 10 mm.

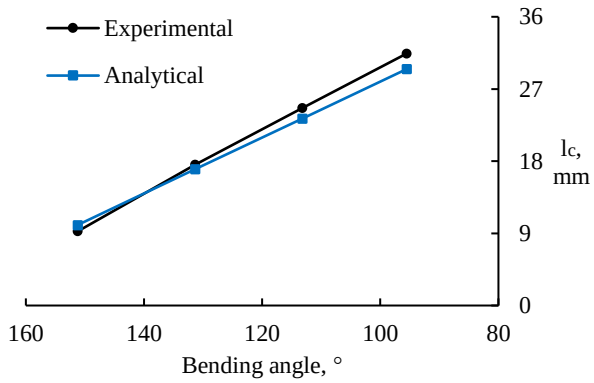

Figure 18 – Comparison of results for contact points position between analytical model and experimental data. Plate: Strenx 700 MC; thickness: 6 mm; die opening: 80 mm; punch radius: 40 mm.

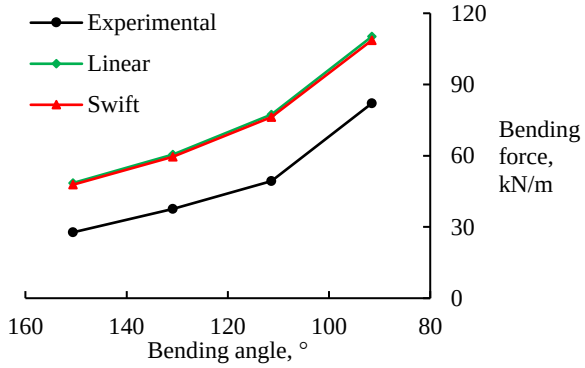

Figure 19 – Comparison of results for the bending force between analytical model and experimental data. Plate: St-37; thickness: 2 mm; die opening: 40 mm; punch radius: 20 mm.

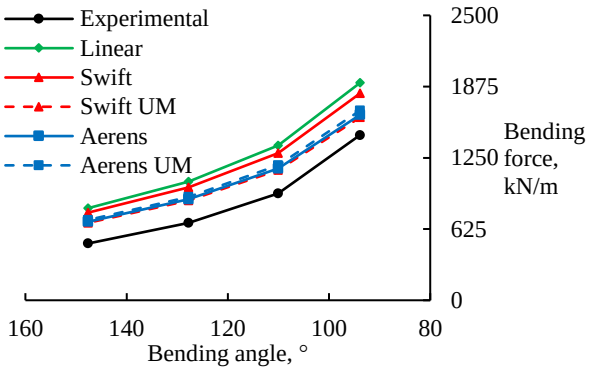

Figure 20 – Comparison of results for the bending force between analytical model and experimental data. Plate: Strenx 1300; thickness: 4 mm; die opening: 60 mm; punch radius: 30 mm.

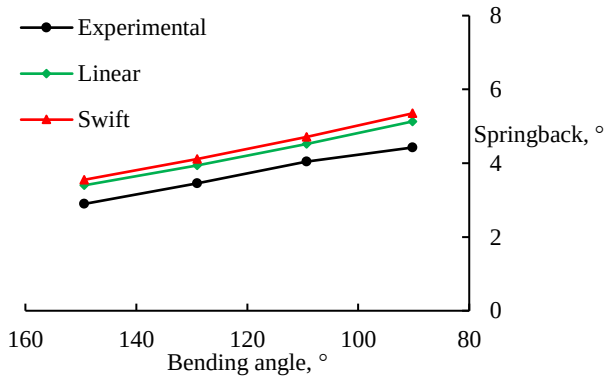

Figure 21 – Comparison of results for the springback angle between analytical model and experimental data. Plate: AISI 316L; thickness: 4 mm; die opening: 40 mm; punch radius: 10 mm.

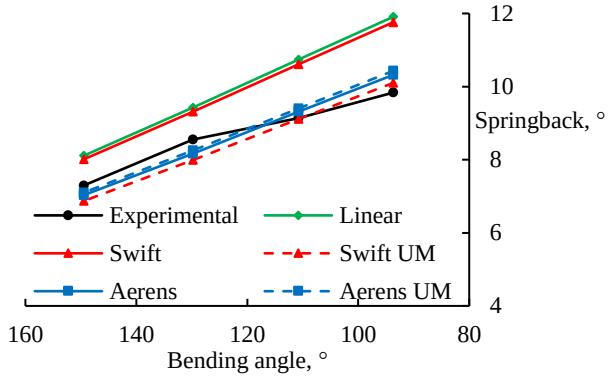

Figure 22 – Comparison of results for springback angle between analytical model and experimental data. Plate: Strenx 700 MC; thickness: 4 mm; die opening: 60 mm; punch radius: 30 mm.

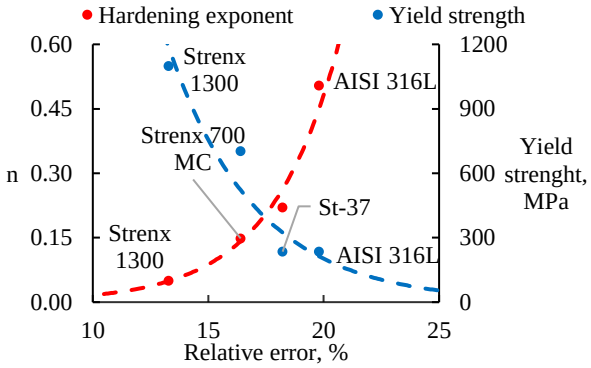

Figure 23 – Bend allowance depends on the hardening exponent and yield strength.

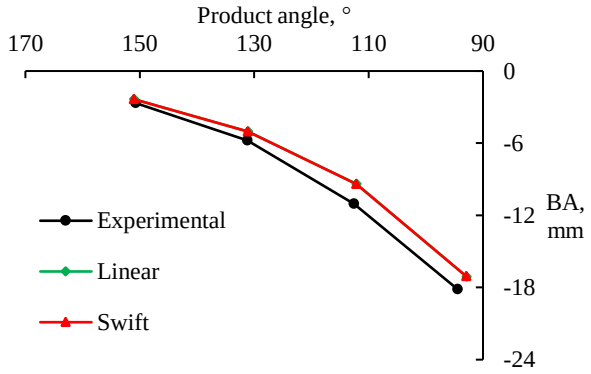

Figure 24 – Comparison of results for bend allowance position between analytical model and experimental data. Plate: St-37; thickness: 8 mm; die opening: 80 mm; punch radius: 20 mm.

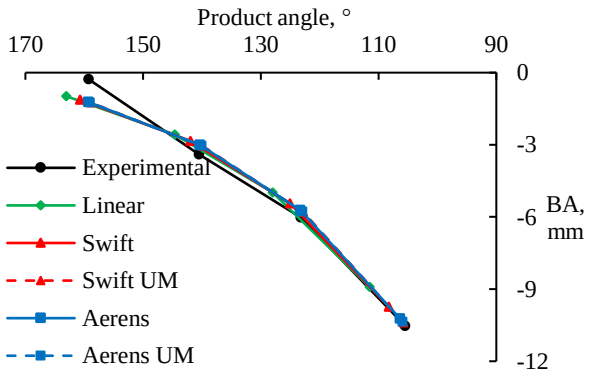

Figure 25 – Comparison of results for bend allowance position between analytical model and experimental data. Plate: Strenx 1300 MC; thickness: 6 mm; die opening: 60 mm; punch radius: 20 mm.

Table list

Table 1
Material parameters according to the linear and Swift laws.

Material	E, GPa	E_{sec}, GPa	A, MPa	B, MPa	K_S, MPa	n_S	ε_{0S}	t, mm
St-37 [9]	220	162	333.1	699.3	659	0.220	0.021	2, 4, 6 and 8
AISI 304 [9]	220	145	362.2	1771.2	1491	0.511	0.044	2
AISI 316L [21]	193	134	339.6	1571.4	1337	0.504	0.048	4, 6 and 8
Strenx 700 MC [17]	205	188	786.7	2134.1	1088	0.073	0.007	4 and 6
Strenx 1300 [17]	197.5	182	1299.3	9503.6	2540	0.133	0.000	4 and 6

Table 2
Material parameters according to the Aerens law.

Material	K_A, MPa	n_A	ε_{0A}	σ_{el}, MPa	ε_{el}	t, mm
Strenx 700 MC [17]	1253	0.140	0.034	702.8	0.0034	4 and 6
Strenx 1300 [17]	2138	0.081	0.000	1098.4	0.0056	4 and 6

Table 3
Material parameters defined by unit moment coefficients of the Swift-like law.

Material	C'', MPa	n	ε_d
Strenx 700 MC	331.4	0.148	0.000
Strenx 1300	495.0	0.050	0.000

Table 4
Material parameters defined by unit moment coefficients of the Aerens-like law.

Material	C'', MPa	n	ε_d	E_b , MPa	σ^*_{el}	$\varepsilon_{b\,el}$
Strenx 700 MC	302.0	0.109	0.008	37546	112.6	0.003
Strenx 1300	450.0	0.000	0.000	36123	180.6	0.005

Table 5
Scheme of experimental plan.

Material / Parameter	St-37	AISI 304/ AISI 316	Strenx 700 MC	Strenx 1300
Bending angle[a]	4	4	4	4[b]
Thickness	4	4	2 (4 and 6 mm)	2 (4 and 6 mm)
Punch radius	4	4	4	4
Die opening	4	4	4	4
Total	174	174	87	80

[a] – 110°, 130°, 150° for t = 6 mm, R_p = 20 mm, w_0 = 40 mm due to geometrical restrictions
[b] – 130°, 150° for t = 6 mm, R_p = 10 mm due to lack of cold formability

Table 6
Maximal standard errors for the selected test cases [28].

Bending characteristic	Number of repetitions	Mean value	± Standard error
Contact points position	5	15.25	±0.77 mm
Springback	3	11.64	±0.71°
Bending force	3	1677.13	±24.24 kN/m
Bend allowance	3	-10.55	±0.55 mm

Table 7
Overview of comparison of the analytical model with experimental data for the contact points position (Equation 4).

Comparison parameter	Material			
	St-37	AISI 304/AISI 316	Strenx 700 MC	Strenx 1300
R^2	0.9663	0.9616	0.9745	0.9719
ε_{av}, *mm*	1.2662	1.4251	0.9710	1.0218
ε_{rel}, *%*	12.804	14.788	9.2460	9.9587
$\bar{\varepsilon}_{av}$, *mm*	-0.4504	-0.7331	0.2107	-0.4303
$\sigma_{\bar{\varepsilon}_{av}}$, *mm*	0.1149	0.1208	0.1284	0.1403

Table 8
Overview of comparison of the analytical model with experimental data for the bending force (Equation 25).

		Material			
Model	Comparison parameter	St-37	AISI 304/AISI 316	Strenx 700 MC	Strenx 1300
Linear	R^2	0.9814	0.9719	0.9687	0.9249
	ε_{av}, *kN/m*	68.074	118.11	174.39	680.74
	ε_{rel}, *%*	22.344	33.443	29.881	65.471
	$\bar{\varepsilon}_{av}$, *kN/m*	-64.490	-116.69	-174.38	-680.74
	$\sigma_{\bar{\varepsilon}_{av}}$, *kN/m*	5.1722	10.358	10.888	48.731
Swift	R^2	0.9811	0.9741	0.9846	0.9893
	ε_{av}, *kN/m*	71.222	132.01	107.49	380.60
	ε_{rel}, *%*	23.378	37.504	18.418	36.605
	$\bar{\varepsilon}_{av}$, *kN/m*	-68.091	-131.33	-106.64	-380.60
	$\sigma_{\bar{\varepsilon}_{av}}$, *kN/m*	5.4164	11.272	5.8606	20.749
Aerens	R^2	-	-	0.9821	0.9911
	ε_{av}, *kN/m*	-	-	62.704	203.43
	ε_{rel}, *%*	-	-	10.744	19.565
	$\bar{\varepsilon}_{av}$, *kN/m*	-	-	-47.133	-203.43
	$\sigma_{\bar{\varepsilon}_{av}}$, *kN/m*	-	-	5.9515	10.210
Swift UM	R^2	-	-	0.9815	0.9907
	ε_{av}, *kN/m*	-	-	57.755	152.92
	ε_{rel}, *%*	-	-	9.8962	14.707
	$\bar{\varepsilon}_{av}$, *kN/m*	-	-	-38.211	-152.81
	$\sigma_{\bar{\varepsilon}_{av}}$, *kN/m*	-	-	6.1823	8.1802
Aerens UM	R^2	-	-	0.9840	0.9890
	ε_{av}, *kN/m*	-	-	58.214	172.82
	ε_{rel}, *%*	-	-	9.9749	16.621
	$\bar{\varepsilon}_{av}$, *kN/m*	-	-	-39.458	-172.72
	$\sigma_{\bar{\varepsilon}_{av}}$, *kN/m*	-	-	5.8406	9.4727

Table 9
Overview of comparison of the analytical model with experimental data for springback (Equation 27).

Model	Comparison parameter	Material			
		St-37	AISI 304/AISI 316	Strenx 700 MC	Strenx 1300
Linear	R^2	0.8118	0.8976	0.9127	0.7874
	ε_{av}, °	0.9395	0.9335	1.3845	5.2548
	ε_{rel}, %	22.875	17.322	19.262	37.417
	$\bar{\varepsilon}_{av}$, °	-0.4025	-0.7775	-1.3429	-5.2547
	$\sigma_{\bar{\varepsilon}_{av}}$, °	0.0987	0.0821	0.0848	0.0282
Swift	R^2	0.8228	0.9092	0.9330	0.9752
	ε_{av}, °	0.9043	1.0167	0.8196	2.2191
	ε_{rel}, %	22.019	18.865	11.403	15.801
	$\bar{\varepsilon}_{av}$, °	-0.4004	-0.0898	-0.7168	-2.2190
	$\sigma_{\bar{\varepsilon}_{av}}$, °	0.0918	0.0756	0.0779	0.1017
Aerens	R^2	-	-	0.9271	0.9800
	ε_{av}, °	-	-	0.4358	0.5252
	ε_{rel}, %	-	-	6.0634	3.7400
	$\bar{\varepsilon}_{av}$, °	-	-	0.0257	-0.2428
	$\sigma_{\bar{\varepsilon}_{av}}$, °	-	-	0.0716	0.0736
Swift UM	R^2	-	-	0.9254	0.9752
	ε_{av}, °	-	-	0.4480	0.5634
	ε_{rel}, %	-	-	6.2324	4.0117
	$\bar{\varepsilon}_{av}$, °	-	-	0.1349	0.2747
	$\sigma_{\bar{\varepsilon}_{av}}$, °	-	-	0.0729	0.0752
Aerens UM	R^2	-	-	0.9316	0.9751
	ε_{av}, °	-	-	0.4370	0.5887
	ε_{rel}, %	-	-	6.0797	4.1921
	$\bar{\varepsilon}_{av}$, °	-	-	0.0785	0.0055
	$\sigma_{\bar{\varepsilon}_{av}}$, °	-	-	0.0692	0.0877

Table 10
Overview of comparison of the analytical model with experimental data for the bend allowance (Equation 30).

Model	Comparison parameter	Material			
		St-37	AISI 304/AISI 316	Strenx 700 MC	Strenx 1300
Linear	R^2	0.9260	0.9222	0.9153	0.9714
	ε_{av}, *mm*	1.2355	1.2940	1.0039	0.8221
	ε_{rel}, *%*	18.256	19.587	17.546	19.974
	$\bar{\varepsilon}_{av}$, *mm*	-1.0189	-1.1016	-0.7191	-0.7132
	$\sigma_{\bar{\varepsilon}_{av}}$, *mm*	0.1439	0.1415	0.1787	0.0828
Swift	R^2	0.9268	0.9228	0.9198	0.9811
	ε_{av}, *mm*	1.2332	1.3079	0.9389	0.5466
	ε_{rel}, *%*	18.222	19.797	16.410	13.280
	$\bar{\varepsilon}_{av}$, *mm*	-1.0180	-1.1215	-0.6323	-0.3787
	$\sigma_{\bar{\varepsilon}_{av}}$, *mm*	0.1435	0.1419	0.1734	0.0638
Aerens	R^2	-	-	0.9143	0.9822
	ε_{av}, *mm*	-	-	0.8959	0.3798
	ε_{rel}, *%*	-	-	15.686	9.2270
	$\bar{\varepsilon}_{av}$, *mm*	-	-	-0.5026	-0.1131
	$\sigma_{\bar{\varepsilon}_{av}}$, *mm*	-	-	0.1714	0.0524
Swift UM	R^2	-	-	0.9135	0.9829
	ε_{av}, *mm*	-	-	0.8915	0.3850
	ε_{rel}, *%*	-	-	15.581	9.3536
	$\bar{\varepsilon}_{av}$, *mm*	-	-	-0.4833	-0.0478
	$\sigma_{\bar{\varepsilon}_{av}}$, *mm*	-	-	0.1712	0.0503
Aerens UM	R^2	-	-	0.9158	0.9830
	ε_{av}, *mm*	-	-	0.8883	0.3665
	ε_{rel}, *%*	-	-	15.525	8.9044
	$\bar{\varepsilon}_{av}$, *mm*	-	-	-0.4975	-0.0926
	$\sigma_{\bar{\varepsilon}_{av}}$, *mm*	-	-	0.1703	0.0516